Developmental Cell
Article

LDL Cholesterol Recycles to the Plasma Membrane via a Rab8a-Myosin5b-Actin-Dependent Membrane Transport Route

Kristiina Kanerva,[1,3,7] Riikka-Liisa Uronen,[1,7,8] Tomas Blom,[1,3] Shiqian Li,[1,3] Robert Bittman,[4] Pekka Lappalainen,[2] Johan Peränen,[2] Graça Raposo,[5,6] and Elina Ikonen[1,3,*]
[1]Institute of Biomedicine, Anatomy
[2]Institute of Biotechnology
University of Helsinki, FI-00014 Helsinki, Finland
[3]Minerva Foundation Institute for Medical Research, FI-00290 Helsinki, Finland
[4]Department of Chemistry and Biochemistry, Queens College of The City University of New York, Flushing, NY 11367-1597, USA
[5]Institut Curie, Centre de Recherche, F-75248 Paris, France
[6]Structure and Membrane Compartments, Centre National de la Recherche Scientifique, Unité Mixte de Recherche 144, F-75248 Paris, France
[7]These authors contributed equally to this work
[8]Current address: Department of Molecular Neurobiology, Max Planck Institute of Experimental Medicine, 37075 Göttingen, Germany
*Correspondence: elina.ikonen@helsinki.fi
http://dx.doi.org/10.1016/j.devcel.2013.09.016

SUMMARY

Mammalian cells acquire cholesterol, a major membrane constituent, via low-density lipoprotein (LDL) uptake. However, the mechanisms by which LDL cholesterol reaches the plasma membrane (PM) have remained obscure. Here, we applied LDL labeled with BODIPY cholesteryl linoleate to identify this pathway in living cells. The egress of BODIPY cholesterol (BC) from late endosomal (LE) organelles was dependent on acid lipase and Niemann-Pick C1 (NPC1) protein, as for natural cholesterol. We show that NPC1 was needed to recruit Rab8a to BC-containing LEs, and Rab8a enhanced the motility and segregation of BC- and CD63-positive organelles from lysosomes. The BC carriers docked to the cortical actin by a Rab8a- and Myosin5b (Myo5b)-dependent mechanism, typically in the proximity of focal adhesions (FAs). LDL increased the number and dynamics of FAs and stimulated cell migration in an acid lipase, NPC1, and Rab8a-dependent fashion, providing evidence that this cholesterol delivery route to the PM is important for cell movement.

INTRODUCTION

Mammalian cells acquire cholesterol, a key membrane constituent, via receptor-mediated endocytosis of low-density lipoprotein (LDL; Brown and Goldstein, 1986). Cholesteryl fatty acid esters, the major constituent of LDL cholesterol, are hydrolyzed by lysosomal acid lipase (LAL) to free cholesterol. The recycling compartments and late endosomes (LE)/multivesicular bodies (MVB) harbor substantial amounts of cholesterol, whereas lysosomes (LY) are cholesterol-poor (Möbius et al., 2003), implying that cholesterol sorting takes place during degradative trafficking. NPC1 and NPC2 proteins are crucial for late endosomal cholesterol egress (Deffieu and Pfeffer, 2011; Kwon et al., 2009). They are thought to act in concert to mediate the removal of unesterified cholesterol, with intraendosomal NPC2 delivering cholesterol to the membrane-bound NPC1 (Kwon et al., 2009).

After liberation from endocytic circuits, LDL cholesterol is routed to other membranes, including the plasma membrane (PM) and endoplasmic reticulum (ER; Ikonen, 2008). Cholesterol was shown to be transported by vesicular trafficking from the NPC1 compartment to the trans-Golgi network (TGN) en route to the ER (Urano et al., 2008). In addition, ORP5, Hrs/Vps27, and Vps4 have been implicated in LDL cholesterol transport to the ER (Du et al., 2011, 2012, 2013). Pharmacological studies indicate distinct routes for cholesterol delivery from the NPC1 compartment to the ER and PM (Wojtanik and Liscum, 2003). However, the mechanism(s) by which LDL cholesterol reaches the PM are unknown.

We have established a fluorescent cholesterol analog (i.e., BODIPY cholesterol [BC]) as a tool to visualize sterol movement in living cells, and showed that the membrane partitioning and trafficking properties of BC resemble those of cholesterol (Blom et al., 2010; Hölttä-Vuori et al., 2008; Jansen et al., 2011). Here we synthesized a BC esterified with linoleic acid, BODIPY cholesteryl linoleate (BC LN), incorporated it into LDL, and characterized the route of LDL-derived sterol delivery to the PM in living cells. We identified Rab8a with its interaction partners as key regulators of endosomal egress and PM delivery of LDL cholesterol. This route appears important for cholesterol delivery to focal adhesions (FAs) and regulation of FA dynamics in the leading edge of migrating cells.

RESULTS

BC LN Visualizes LDL-Derived Sterol Trafficking in Living Cells

We labeled human LDL with BC LN (Figures 1A and 1B). A431 cells were preloaded with dextran to visualize LE/LY, and then

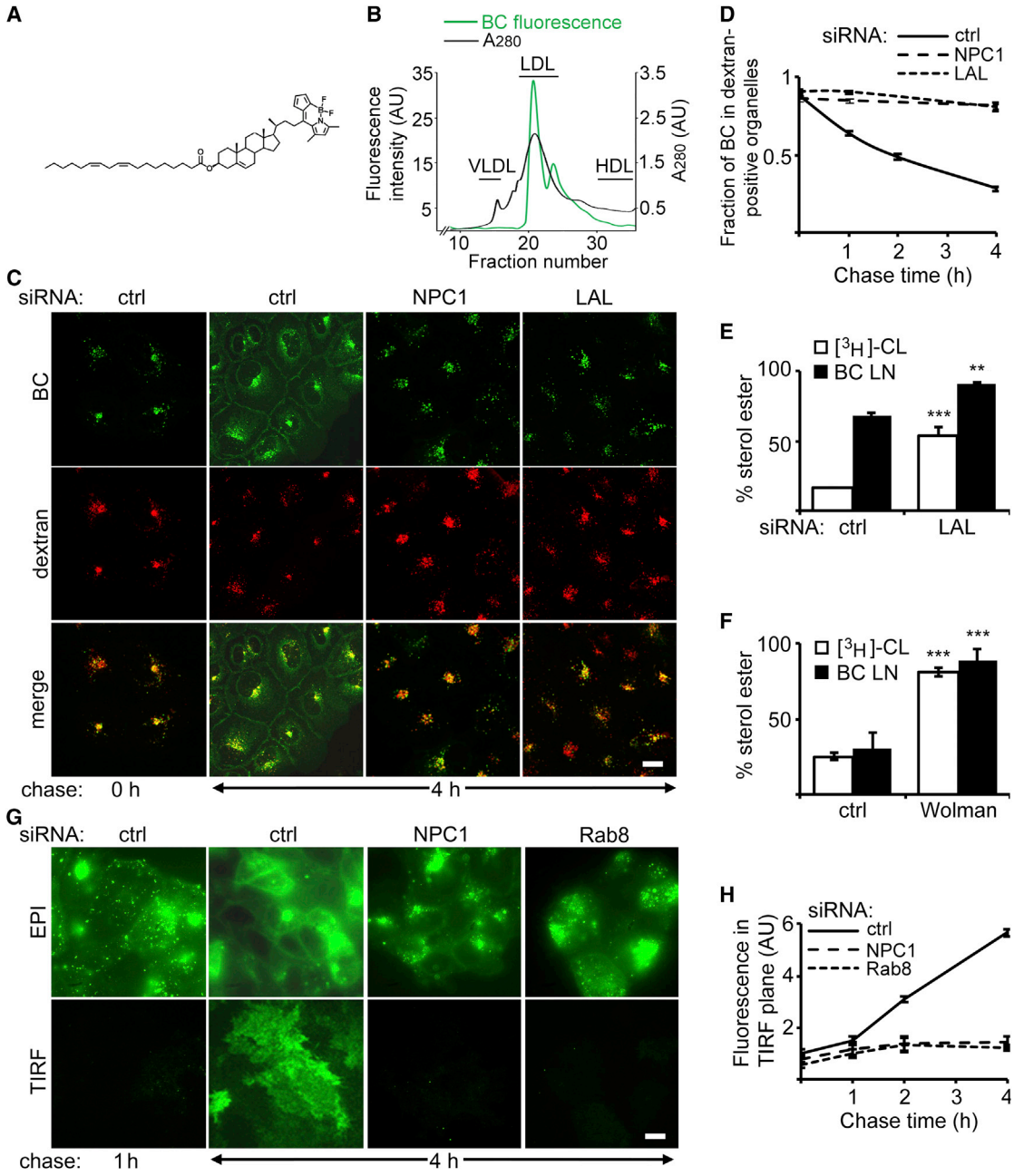

Figure 1. BODIPY Cholesteryl Linoleate-Labeled LDL Is a Suitable Tool to Trace the Trafficking of LDL-Derived Sterol in Living Cells

(A) Structure of BODIPY cholesteryl linoleate (BC LN).

(B) Chromatographic profile of the distribution of BC fluorescence after gel filtration of BC LN-labeled LDL. Lines indicate the typical distribution profiles of the main lipoprotein classes after fractionation from plasma (very-low-density lipoprotein fractions 13–17; LDL 18–24; high-density lipoprotein 27–33).

(C) Confocal images of A431 cells transfected with the indicated siRNAs, labeled overnight with dextran followed by pulse-labeling with BC LN-LDL, and imaged after 0 hr and 4 hr of chase. Scale bar, 10 μm.

(D) Quantification of the fraction of BC fluorescence residing in dextran-positive organelles during the chase (n = 14 independent experiments, N = 170–360 cells [control], N = 33–46 cells [LAL and NPC], mean ± SEM, compared to control).

(E and F) Analysis of cholesteryl ester hydrolysis in A431 cells transfected with the indicated siRNAs (E) or in control and Wolman disease patient fibroblasts (F). The cells were pulse-labeled with [^{3}H]-CL LDL or BC LN-LDL for 1 hr (A431) or 7 hr (fibroblasts) and chased for 2 hr (A431) or 17 hr (fibroblasts), and the fraction of sterol remaining as fatty acid esters after chase is shown (n = 3–7; ***$p < 0.001$; **$p < 0.01$; Student's t test, mean ± SEM, compared to control siRNA or cell line).

(G) TIRF and epifluorescence (EPI) images of A431 cells transfected with the indicated siRNAs and pulse-labeled with BC LN-LDL. Scale bar, 10 μm.

(H) Quantification of BC fluorescence intensity in the TIRF plane as a function of time (n = 3 independent experiments, N = 11–36 cells, mean ± SEM).

See also Figure S1.

pulse-labeled with BC LN-LDL. After 2 hr, the label largely colocalized with dextran-positive LE/LY (Figure 1C). We then incubated the cells for increasing times without label (= chase), during which time BC exited LE/LY and reached the PM (Figure 1C). The fraction of BC fluorescence colocalizing with dextran during chase provided a quantitative measure of BC efflux from LE/LY. A steady decrease in colocalization was observed during a 4 hr chase (Figure 1D).

When cellular BC LN hydrolysis was analyzed, we found that immediately after the labeling, the majority of BC (~60%) was still esterified (i.e., nonhydrolyzed), as compared to ~10% after a 4 hr chase. To test if LAL was responsible for the hydrolysis, we labeled control and LAL-depleted cells with BC LN-LDL or [^{3}H]-cholesteryl linoleate (CL)-LDL and analyzed sterol hydrolysis. After a 2 hr chase, about 15% of [^{3}H]-CL remained esterified in control cells, whereas up to 60% was esterified in LAL-silenced cells (Figure 1E). The hydrolysis of BL LN was slower but also LAL-sensitive, with ~60% and ~90% remaining as intact BC LN in control and LAL knockdown cells, respectively. In vitro hydrolysis confirmed that BC LN was hydrolyzed more slowly than [^{3}H]-CL (Figure S1A available online). In the fibroblasts from a patient with Wolman disease (LAL-deficient), hydrolysis of both labels was inhibited (Figure 1F). Together, these results provide evidence that BC LN is hydrolyzed by LAL.

Efflux of BC from LE/LY Depends on LAL, NPC1, and Microtubules

To analyze whether the LE/LY exit of BC LN-LDL is dependent on LAL and NPC1, we followed its egress in cells depleted of these proteins. After 4 hr of chase, BC still colocalized with dextran as extensively as at the beginning of chase in both LAL- and NPC1-deficient cells (Figures 1C and 1D). Microtubule depolymerization by nocodazole during the chase also prevented BC exit from LE/LY (Figure S1B). To visualize BC arrival at the PM, we used total internal reflection fluorescence (TIRF) microscopy. In control cells, no BC was observed in the TIRF plane at early chase times but BC fluorescence intensity increased during chase (Figures 1G and 1H). In contrast, in NPC1-depleted cells, no increase in BC fluorescence intensity in the TIRF plane was observed (Figures 1G and 1H). This is in agreement with defective PM arrival of LDL cholesterol in NPC1-silenced cells, as measured by oxidation of LDL-derived [^{3}H]-CL (Figures S1C and S1D). Together, these findings indicate that the egress of LDL-derived BC from the LE/LY and its arrival in the PM depend on NPC1.

Rab GTPases in LE/LY Cholesterol Trafficking

Rab GTPases have been implicated in cholesterol trafficking (Choudhury et al., 2004; Hölttä-Vuori et al., 2000, 2002; Walter et al., 2003) and LDL-derived BC was found to move in vesicular structures during chase (Movie S1). Therefore, we silenced candidate Rabs involved in endosomal/Golgi trafficking to assess their involvement in LDL-sterol transport using the BC LN-LDL pulse-chase assay. As expected, depletion of early endosomal Rab4 or Rab5 diminished BC LN-LDL uptake (Figure S2A), while in Rab7-depleted cells, BC LN-LDL did not efficiently reach dextran-positive LE/LY (Figures S2B and S2C).

In the remaining Rab siRNAs tested, BC LN reached dextran positive LE/LY. In Rab8- (Rab8 refers hereafter to Rab8a) or Rab9-depleted cells, its removal from LE/LY was defective (Figures 2A and 2B). Rab9 regulates LE-TGN (Ganley and Pfeffer, 2006; Lombardi et al., 1993) and Rab8 exocytic/recycling transport (Hattula et al., 2006; Peränen et al., 1996). The PM arrival of both BC and [^{3}H]-cholesterol derived from LDL hydrolysis was defective in Rab8-depleted cells, as assessed by TIRF microscopy and PM cholesterol oxidation, respectively (Figures 1G, 1H, S1C, and S1D). In addition, total cholesterol content and cholesterol in Lamp1-positive organelles were increased in Rab8-depleted cells analogously to NPC1-depleted cells (Figures 2C, 2D, S2D, and S2E). In Rab8+Rab9-silenced cells, LE/LY BC efflux was more severely compromised than in either silencing alone (Figures 2B, 2E, S2D, and S2E). This suggests that Rab8 and Rab9 are involved in the removal of LDL-cholesterol from LE/LY and regulate different efflux routes.

We also performed the BC LN-LDL pulse-chase assay in cells depleted of Rabin8, a Rab8-specific guanine nucleotide exchange factor (GEF; Hattula et al., 2002), or of ARF6, an upstream regulator of Rab8 (Hattula et al., 2006), as well as in cells overexpressing TBC1D30, a Rab8 GTPase-activating protein (GAP; Yoshimura et al., 2007). Also in these conditions, a larger fraction of BC colocalized with dextran at 4 hr of chase (Figures 2B and 2E). These observations further substantiate Rab8 as a regulator of LE/LY cholesterol egress and suggest that Rab8 GTP cycling is needed.

Recruitment of Rab8 to LE

To study Rab8 localization in LDL-loaded cells, RFP-Rab8 or Cherry-Rab8-expressing cells were labeled with BC LN-LDL. After 3 hr chase, Rab8 and BC partially colocalized in vesicles throughout the cytoplasm (Figures 3A and S3A). Quantification revealed that at this time point ~60% of Rab8-positive vesicular structures (597 out of 976) also contained BC. Interestingly, RFP-Rab8 exhibited a higher degree of colocalization with BC than with dextran (Figure 3B), suggesting that Rab8 is specifically recruited to a subpopulation of LE harboring LDL cholesterol. In NPC1-depleted cells, poor colocalization between RFP-Rab8 and BC was observed (Figures 3B and S3B), providing evidence that Rab8 LE recruitment depends on NPC1. Immunoblotting of NPC1-immunoisolated organelles with Rab8 antibodies further showed that endogenous Rab8 associates with NPC1-containing organelles (Figures 3C and 3D). By immunofluorescence microscopy, endogenous Rab8 staining became more punctate upon LDL loading and localized in domains of CD63-positive organelles (Figures S3C and S3D). Finally, by immuno-electron microscopy of ultrathin cryosections of cells loaded with LDL, we observed the localization of GFP-Rab8 in CD63-positive LE characterized by intraluminal vesicles and multilayered membrane sheets (Figure 3E). Together, these results suggest that Rab8 is recruited to LE upon LDL loading and that this necessitates a functional NPC1 protein.

Rab8 Regulates Actin-Modulated Motility of BC-Containing LE

Cholesterol loading reduces the motility of LE (Chen et al., 2008; Lebrand et al., 2002). We found that in Rab8-depleted cells, organelles containing BC and dextran were mislocalized to the cell periphery, under the leading edge (Figures 2B and 4A) and their motility was strikingly reduced (Movie S1). Therefore, we investigated whether Rab8 overexpression increases the movement of

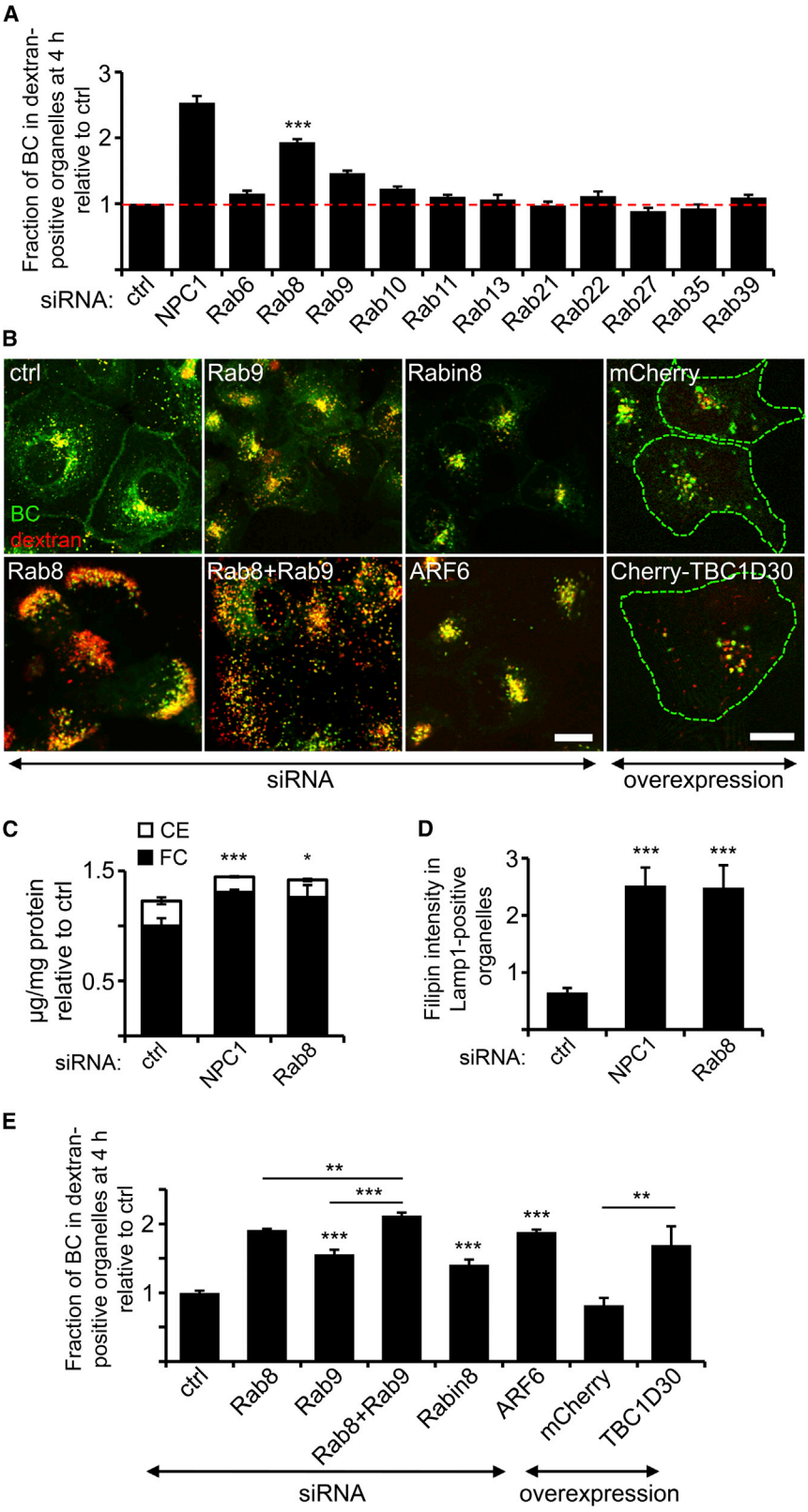

Figure 2. Rab8 Modulates the Egress of Late Endosomal LDL-Derived BC

(A) Quantification of the fraction of BC fluorescence residing in dextran-positive organelles after 4 hr of chase in cells transfected with the siRNAs indicated prior to pulse labeling with BC LN-LDL. (n = 8 independent experiments; N = 31–51 cells; ***p < 0.001; Student's t test, mean ± SEM, compared to control).

(B) Overlaid confocal images of BC and dextran in A431 cells transfected with the indicated siRNAs or cDNA constructs (transfected cells are outlined). The cells were pulse labeled and chased for 4 hr prior to imaging. Scale bar, 10 µm.

(C) TLC analysis of free cholesterol (FC) and esterified cholesterol (CE) amounts of A431 cells transfected with the indicated siRNAs (n = 5–7; ***p < 0.001; *p < 0.05; Student's t test, mean ± SEM). The results were normalized to control, which corresponds to 19.43 ± 1.91 µg/mg protein.

(D) Quantification of filipin fluorescence intensity in A431 cells transfected with the indicated siRNAs (n = 21–23 cells; ***p < 0.001; Student's t test, mean ± SEM).

(E) Quantification of the fraction of BC fluorescence residing in dextran-positive organelles after 4 hr of chase (n = 19–31 cells; ***p < 0.001; **p < 0.01; Student's t test, mean ± SEM, compared to control unless otherwise indicated).

See also Figure S2.

BC-containing LE. Plotting of BC fluorescence intensity against the distance traveled by the organelles revealed that the more BC they contained the less they moved (Figure 4B). No such correlation was observed with dextran intensity (Figure S4A). Interestingly, overexpression of RFP-Rab8 increased the motility of BC-containing organelles, also those with a high BC content (Figures 4B and 4C). The vectorial movement of BC organelles was dependent on actin because Latrunculin A (LatA) treatment increased their motility (Figure 4C). However, LatA did not further stimulate the motility in Rab8-overexpressing cells (Figure 4C), suggesting that Rab8 acts in concert with actin. In Rab8-silenced cells, the cortical actin was disorganized (Figure 4A) and when the cells were treated with LatA or cytochalasin D, the peripheral BC organelles regained their motility and predominant perinuclear positioning (Figures 4C and S4B). These data indicate that Rab8 regulates the actin-dependent motility of BC-containing organelles.

Highly Dynamic CD63-Containing Organelles Transport LDL-Derived BC

To further characterize the BC egressing organelles, we tracked BC efflux in cells overexpressing CD63-Cherry or Lamp1-RFP. While colocalization of BC and dextran/Lamp1 decreased during the chase, BC and CD63-Cherry colocalization remained

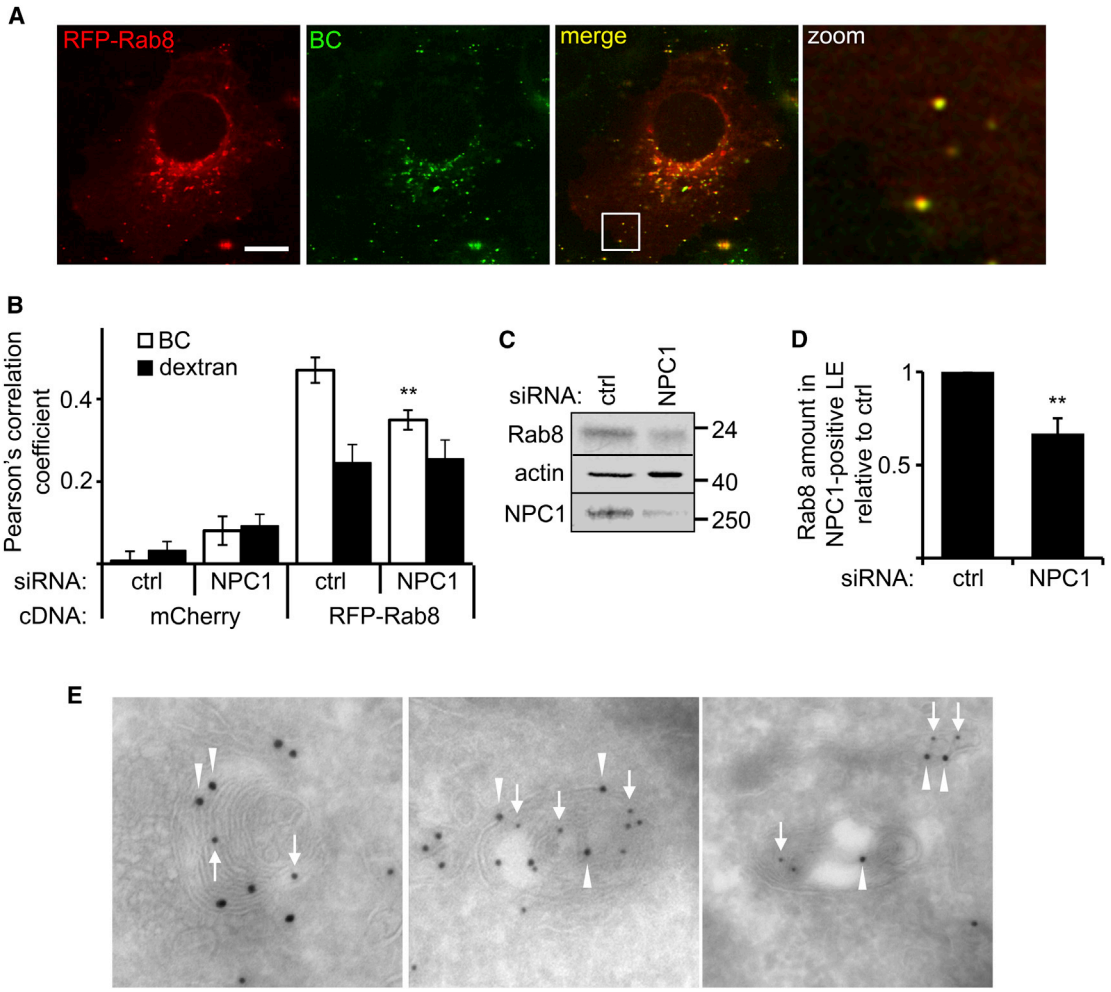

Figure 3. Rab8 Is Recruited to BC-Enriched LE/LY in an LDL- and NPC1-Dependent Manner

(A) Confocal images of A431 cells transfected with control siRNA prior to overexpression of RFP-Rab8 and pulse-labeling with BC LN-LDL. Images were captured after a 2 hr chase. Right panel shows a magnification of the indicated area. Scale bar, 10 μm.

(B) Quantification of colocalization of mCherry or RFP-Rab8 with either BC- or dextran-positive organelles. The cells were transfected with the indicated siRNAs prior to cDNA overexpression and BC LN-LDL pulse-chase labeling, and imaged after 2 hr of chase (n = 14–30 cells; **$p < 0.01$; Student's t test, mean ± SEM, compared to control overexpressing RFP-Rab8).

(C and D) Immunoblot analysis showing Rab8, actin, and NPC1 levels in LE/LY immunoisolated using NPC1 antibodies. The organelles were isolated from A431 cells loaded with LDL after transfection with the indicated siRNAs. (D) Quantification of the amount of Rab8 in NPC1-immunoisolated LE/LY (n = 4; **$p < 0.01$; Student's t test, mean ± SEM).

(E) Immunogold labeling on ultrathin cryosections of A431 cells stably overexpressing GFP-Rab8 shows the presence of GFP-Rab8 (10 nm gold particles, arrows) in CD63 (15 nm gold particles, arrowheads)-containing LE/LY.

See also Figure S3.

essentially unaltered (Figures 4D and S1E). This suggests that BC is transported to the PM in CD63-positive lysosome-related organelles (LRO), from where dextran and Lamp1 are predominantly excluded during sterol egress. In Rab8-depleted cells, the segregation of CD63 and dextran was impaired (Figure 4E). This implies that Rab8 is needed to separate CD63- and cholesterol-enriched LE from the dextran-containing LY.

We used high-resolution time-lapse imaging to study the dynamics of BC- and CD63-harboring organelles. Most were spherical or oval in shape with a diameter of 0.09–1.41 μm (Table S1) and showed extensive fusions and fissions with one another (Movie S2). Often, tubular profiles containing BC emanated from CD63-positive vesicles (Figure 4F). These tubules extended and retracted rapidly and were typically devoid of CD63. The BC vesicles moved with an average velocity of 0.85 μm/s (maximal velocity, 2.76 μm/s), characteristic of microtubule-based motility (Vale and Fletterick, 1997). Most vesicles exhibiting long-distance vectorial motility (158 of 276, i.e., 57% of all BC-positive vesicles tracked), traveling from the perinuclear region to the cell periphery, some moved in the opposite direction, and a few laterally, along the PM. Occasionally, the vesicles stalled and changed speed and/or direction.

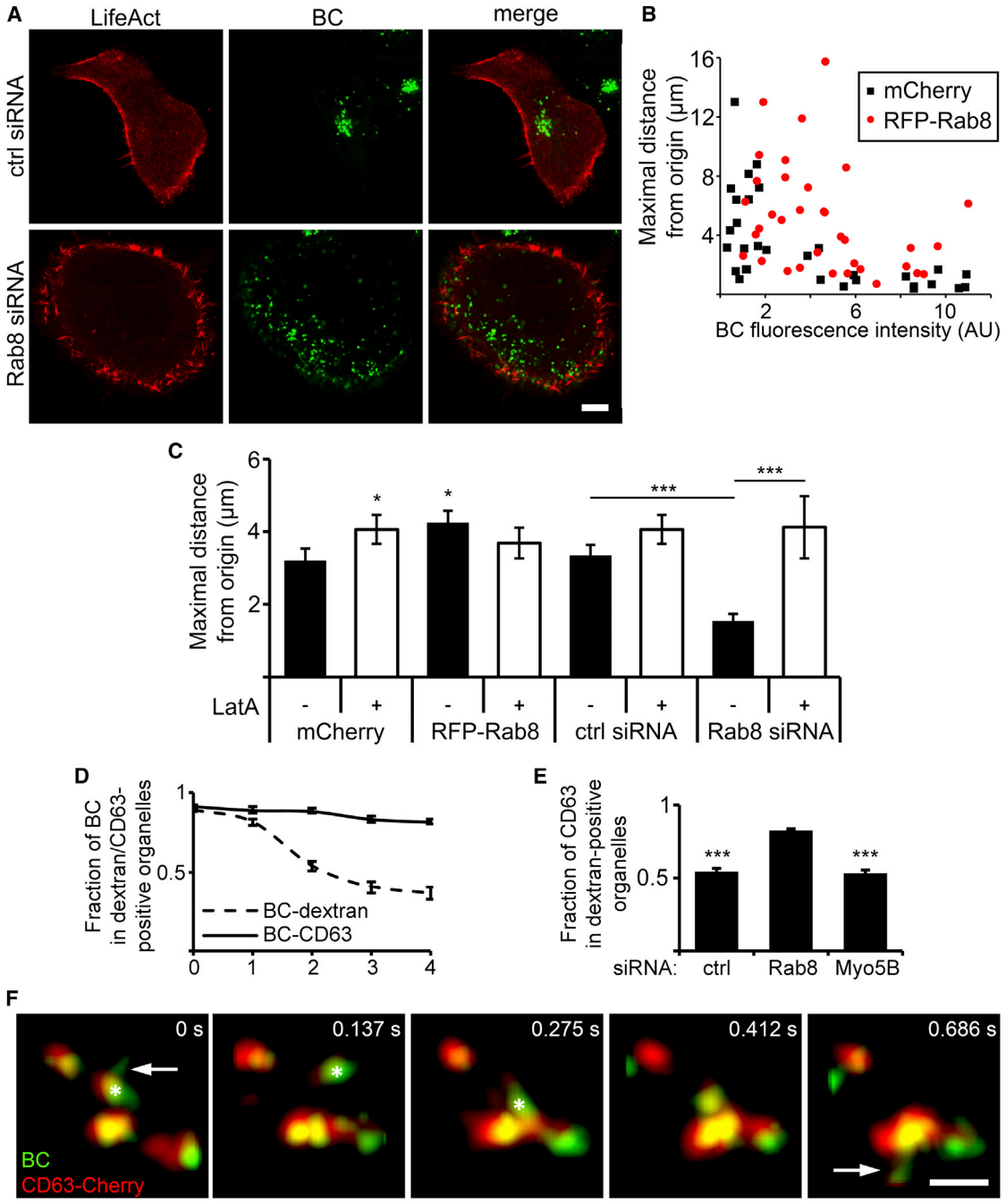

Figure 4. Rab8 Regulates Actin-Dependent Motility of BC-Enriched LE/LY and Promotes Their Segregation

(A) Confocal images showing the localization of BC vesicles in control or Rab8-depleted cells. A431 cells were transfected with the indicated siRNAs prior to LifeAct-RFP overexpression, and then pulse labeled with BC LN-LDL. Time-lapse images were obtained after a 2 hr chase. Scale bar, 10 μm.

(B) Quantification of the distance traveled by the vesicles plotted against their BC fluorescence intensity. A431 cells transfected with the indicated cDNAs were pulse-labeled with BC LN-LDL and time-lapse confocal images were obtained at 1.63 s intervals for 1.5 min after a 2 hr chase (n = 29–34 cells; see also Figure S3E).

(C) Quantification of the distance traveled by BC carriers in BC LN-LDL pulse-labeled A431 cells transfected with either the cDNAs or siRNAs indicated. Time-lapse images were captured at 1.63 s intervals for 1.5 min after 2 hr of chase with (+) or without (−) LatA-treatment. (n = 43–98 cells; ***$p < 0.001$; *$p < 0.05$; Student's t test, mean ± SEM, compared to mCherry − LatA unless otherwise indicated).

(D) Quantification of the fraction of BC fluorescence residing in either CD63- or dextran-positive organelles in CD63-Cherry overexpression cell line pulse-labeled and chased with BC LN-LDL (n = 13–20 cells, mean ± SEM).

(E) Quantification of the fraction of CD63 residing in dextran-positive organelles after 4 hr of chase in CD63-Cherry-overexpressing cells transfected with the indicated siRNAs and pulse-labeled with BC LN-LDL (n = 20–21 cells; ***$p < 0.001$; Student's t test, mean ± SEM, compared to Rab8).

(legend continued on next page)

Myo5b Mediates the Actin-Modulated Motility of BC-Containing LE

To characterize the mechanism of Rab8- and actin-modulated motility of BC carriers, we targeted the Rab8 interaction partner myosin 5 (Myo5). We depleted Myo5b or Myo5c in A431 cells (Myo5a is neuron-specific; Roland et al., 2007, 2009) and assessed the effects on organelle motility and sterol delivery. Depletion of either Myo5 slightly increased BC retention in dextran-positive organelles (Figures 5A and 5B). However, depletion of Myo5b in Rab8-silenced cells exhibited a striking effect, alleviating all the major parameters of the Rab8 silencing phenotype: mislocalization of BC organelles to the leading edge (Figure 5A), their vectorial motility (Figure 5C), and capability to efflux BC (Figure 5B). A similar effect was not observed when Myo5c was codepleted with Rab8 (Figures 5B and S1F). Interestingly, Myo5b silencing did not prevent the segregation of CD63-harboring LE from dextran-containing LY (Figure 4E), suggesting that its effect takes place later. These data strongly suggest that Rab8 regulates the actin-modulated motility of BC-containing organelles via Myo5b.

Delivery of BC Carriers to the PM

When BC vesicle dynamics in the immediate vicinity of the PM was assessed by TIRF microscopy during efflux, we noticed that vesicles in the cell periphery were more confined than in the central area (tracking of 93 peripheral and 151 central vesicles). They moved at slower speed in x-y direction than the central ones (Figures 5D and 5E; Movie S3). They also showed less variance in fluorescence intensity fluctuations in the TIRF plane compared to the perinuclear ones (Figures 5D and 5F), likely reflecting reduced vesicle motility in the z direction. These results suggest that PM docking of BC carriers preferably takes place in the cell periphery.

BC vesicles seemed to arrive in the TIRF plane to peripheral predilection sites occupied by docked BC vesicles (Figure 6A). We therefore considered that they may represent FA. Indeed, tracking of BC vesicles in cells overexpressing the FA marker zyxin-Cherry revealed that the majority of immotile ($\geq$4 s) BC vesicles in the cell periphery were docked to FA (13 of 16 docked vesicles). In addition, ~25% of moving vesicles were communicating transiently with FA (12 of 49 moving vesicles; Figures 6B and 6C; Movie S4). Considering that FA occupy a minor fraction of the PM area, this represents a substantial enrichment of BC vesicles in their vicinity. Interestingly, vinculin staining revealed that LDL-supplementation doubled the number of FA in migrating A431 cells and induced a 2.5-fold increase in their size compared to control (−LDL) cells (Figures 6D, 6E, and S5A). LDL also induced an increased FA turnover as assessed by GFP-paxillin fluorescence intensity fluctuations of individual FA (Figures 6F and 6G; Movie S5). In LDL-supplemented cells, most FA assembled and disassembled rapidly, while in its absence, FAs were either stable or disassembled during the 1h recording (Figures 6F and 6G; Movie S5). These results indicate that the morphology and dynamics of FA are regulated by LDL.

LDL-Derived Cholesterol Stimulates Cell Migration

Taken the striking effects of LDL on FA, we studied whether LDL also affects cell migration in a wound healing assay. Time-lapse imaging showed that the trajectories of A431 cells supplemented with LDL immediately after wounding were longer than those incubated in its absence (Figure 7A). When wound closure was analyzed after 24 hr, the LDL-supplemented cells had migrated almost twice as far as those without LDL (Figures 7B and 7C). This stimulatory effect of LDL was preserved in the presence of mitomycin C (Figure S5B), indicating that it was not due to enhanced cell division. Depletion of either LAL or NPC1 abolished the stimulatory effect of LDL (Figures 7B and 7C), indicating that the hydrolysis of esterified LDL-cholesterol and subsequent liberation of free cholesterol from LE are prerequisites for the stimulatory effect of LDL on cell migration. The migration of Rab8 depleted cells was severely attenuated both in the absence and presence of LDL and no stimulatory effect of LDL was observed (Figure 7C).

To study the role of Rab8 and its GTP-binding status on cell motility in another model, we repeated the wound healing assay in HT1080 fibrosarcoma cells overexpressing the GTP-bound Rab8-Q67L or the GDP-bound Rab8-T22N mutant. In wild-type HT1080 cells, LDL supplementation increased wound healing analogously to A431 cells (Figure 7D). In Rab8-Q67L-expressing cells, migration was enhanced compared to control cells both in the absence and presence of LDL. In contrast, the Rab8-T22N expressing cells did not increase motility in response to LDL, despite high basal motility (Figure 7D). Silencing of endogenous Rab8 from wild-type HT1080 cells also abolished the stimulatory effect of LDL (Figure 7D). These findings suggest that Rab8-GTP controls the LDL-dependent motility of fibrosarcoma cells. Importantly, although both A431 and HT1080 cells are capable of synthesizing cholesterol, this did not compensate for the lack of LDL cholesterol during cell migration.

DISCUSSION

Cells regulate material uptake from the extracellular environment via receptor-mediated endocytosis. This concept was originally established using LDL uptake as the paradigm (Brown and Goldstein, 1986). LDL uptake is increased when cells need cholesterol, and the quantitatively major function of cholesterol is to serve as a membrane constituent, especially in the PM. Despite major advances in our understanding of endosomal trafficking, the mechanism of LDL cholesterol redelivery to the PM has remained open. Biochemical studies indicated that cholesterol exits the LE/LY after ester hydrolysis and reaches the PM and the ER (Ikonen, 2008), but the lack of suitable live tracers for sterol imaging has impeded the visualization of its postendosomal itinerary.

Here, we used a BC derivative, BC LN, to label LDL and to record high-resolution time-lapse images of postendosomal sterol transport in living cells. We show that the endosomal exit of BC LN necessitates that it is hydrolyzed by LAL and mobilized by

(F) Selected still images from a high frame-rate recording of BC vesicle dynamics in stable CD63-Cherry cell line pulse-labeled with BC-LN LDL and chased for 2 hr. Images represent two-dimensional projections of time-lapse z-stacks. Arrows indicate BC tubules emanating from CD63-positive organelles and asterisks a BC-containing vesicle fusing with another one. Scale bar, 1 μm.
See also Figure S4, Movies S1 and S2, and Table S1.

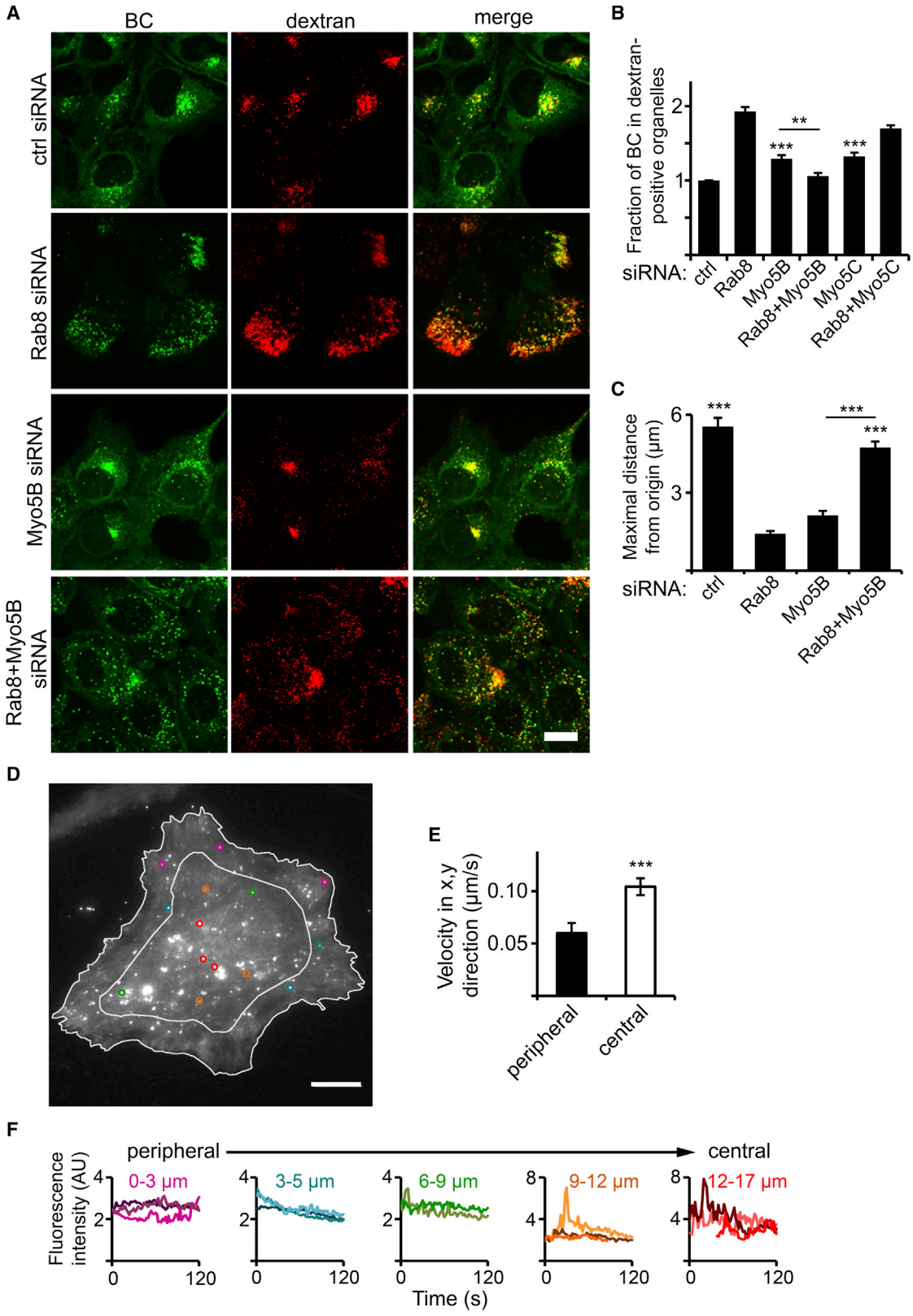

Figure 5. Docking of BC-Harboring Organelles to the PM upon Myo5b-Mediated Association of Vesicles with Cortical Actin

(A) Confocal images of A431 cells transfected with the indicated siRNAs prior to pulse-labeling with BC LN-LDL. The cells were imaged after 4 hr of chase. Scale bar, 10 μm.

(legend continued on next page)

NPC1. This argues that the compound follows the itinerary of native cholesterol, despite its slower hydrolysis compared to native cholesterol. The majority of cholesterol in LDL is esterified to a fatty acid, with oleate and linoleate representing the most abundant species. Notably, lysosomal hydrolysis of BC oleate (Röhrl et al., 2012) was significantly slower than that of BC LN, making it less suitable for this study (R.-L.U. and E.I., unpublished data). This agrees with the fact that the hydrolysis of LDL CL is faster than that of LDL cholesteryl oleate (Slotte and Bierman, 1988).

By candidate screening, we identified Rab8 with its up- and downstream interactors (ARF6, Rabin8, TBC1D30, and Myo5b) as regulators of postendosomal sterol transport. Silencing of Rab8 itself, or ARF6 or Rabin8 upstream of it, impeded this process as did overexpression of the Rab8 GTPase activator TBC1D30. Biochemical experiments using [^{3}H]-CL confirmed that LE-PM cholesterol delivery was disturbed in Rab8-depleted cells. A major role of Rab8 in this route agrees with our previous observations on the role of Rab8 in cholesterol overloaded cells: Rab8 overexpression rescued lysosomal cholesterol accumulation in NPC1-deficient cells (Linder et al., 2007) and stimulated cholesterol efflux to the physiological acceptor apoA-I in macrophage foam cells (Linder et al., 2009).

Rab8 localizes to the PM, Golgi complex, and endosomal compartments (Chabrillat et al., 2005; Hattula et al., 2002, 2006; Vaibhava et al., 2012). We provide evidence that LDL loading modifies Rab8 distribution, with some of the protein directed to LE, provided that NPC1 is functional. Rab8 facilitated the vectorial movement of BC carriers and possibly thereby assisted their segregation from (dextran-containing) LY. This agrees with the idea that cholesterol leaves LE prior to their fusion with terminal LY (Gallala and Sandhoff, 2011). The BC-containing pleiomorphic carriers/LROs also harbored the tetraspanin CD63, known to be enriched in the PM and in the internal membranes of MVBs that give rise to exosomes (Kobayashi et al., 2000; Pols and Klumperman, 2009). Despite extensive colocalization, CD63 appeared to be dispensable for LE exit and PM arrival of BC as this process was not affected by CD63 silencing (K.K. and E.I., unpublished data). Interestingly, the machineries employed for the PM delivery of LDL cholesterol and for exosome secretion may share similar components. For instance, Rab27 that regulates exosome secretion (Ostrowski et al., 2010) interacts with synaptotagmin-like protein-4a, rabphilin, and Noc2 that are also Rab8 interactors (Fukuda, 2013).

Some of the LDL cholesterol moves from the NPC1 compartment to the TGN, as reported by Urano et al. (2008). We did not see any obvious Golgi-like labeling with BC during the pulse-chase assay in A431 cells, but some of the sterol probably moves from LE to the TGN, and our data suggest Rab9 as a candidate to control this route. Remarkably, in other cell types such as primary human fibroblasts, a clear Golgi labeling pattern can be observed during LDL-derived BC egress (K.K. and E.I., unpublished data). This suggests that the routes of LDL cholesterol delivery downstream of LE may vary between cell types.

The BC organelles utilized both microtubules and actin for movement, and eventually became immobilized in the cell periphery by a Myo5b-dependent mechanism that anchored the carriers to the cortical actin. Interestingly, a Rab8-Myo5b transport process has been described in ciliary biogenesis, apical lumen formation, and stretch-induced secretion (Bryant et al., 2010; Khandelwal et al., 2013; Nachury et al., 2007; Sato et al., 2007), and the homologous Sec4p-Myo2p pathway has been implicated in yeast exocytosis (Donovan and Bretscher, 2012; Santiago-Tirado et al., 2011). Both the apical membrane of epithelial cells and the primary cilium are cholesterol-dependent membrane specializations. Thus, it seems logical that cholesterol is cotransported with select proteins targeted to such domains. However, it is likely that Rab8 can also control the delivery of proteins to specialized membrane domains independently of its role in cholesterol transport.

How Myo5b is recruited to or removed from the cholesterol-enriched carriers is not known but the mechanism might be analogous to that in yeast (Donovan and Bretscher, 2012): Myo2p (Myo5 homolog) is recruited to the vesicle and activated; after enrolling the exocyst complex and GTP-bound Sec4 (Rab8 homolog), the vesicles are tethered to the PM, and subsequent hydrolysis of Sec4-GTP enables the recycling of Myo2p from the bud site back to the mother cell. Of note, Rab11 has been implicated as an upstream regulator of Rab8 in Rab8-Myo5b-dependent transport processes (Bryant et al., 2010; Knödler et al., 2010; Roland et al., 2011; Westlake et al., 2011). However, we observed no effect on LE-PM delivery of LDL-derived BC upon Rab11 silencing, arguing that Rab11 was dispensable for this process (K.K. and E.I., unpublished data).

By using TIRF microscopy, we did not observe clear fusion events of the BC carriers with the PM, as has been observed with exocytic proteins (Keller et al., 2001; Letinic et al., 2009). This might be due to a kiss-and-run type of interaction of the BC vesicles with the PM and/or the rapid lateral diffusion of BC upon PM arrival. Remarkably, the BC carriers were not homogeneously delivered to the entire basal PM. Rather, they were preferably delivered to the sites of FA, particularly in the leading edge. Indeed, CD63 interacts with several integrins, and the tetraspanin complexes cluster in cholesterol-rich microdomains that control adhesive and migratory properties of cells (Pols and Klumperman, 2009). Our observations that LDL increased

(B) Quantification of the fraction of BC fluorescence residing in dextran-positive organelles after 4h chase (n = 3 independent experiments; N = 20–56 cells; ***p < 0.001; **p < 0.01; Student's t test, mean ± SEM, compared to control unless otherwise indicated).
(C) Quantification of the distance traveled by BC carriers. The cells were prepared as in Figure 5A and time-lapse confocal images were acquired at 1.63 s intervals for 1.5 min after a 2 hr chase (n = 100–109 organelles in 4–5 cells; ***p < 0.001; Student's t test, mean ± SEM, compared to Rab8 unless otherwise indicated).
(D) Representative TIRF image of A431 cell pulse-labeled with BC LN-LDL and chased for 2 hr. The outer line indicates the cell edge and the interior line an ~5 μm distance from the edge used in quantifications to classify the BC vesicles as either peripheral or central. Scale bar, 10 μm.
(E) Quantification of the velocity of BC vesicles in x-y direction in the TIRF plane (n = 22 vesicles in two cells; ***p < 0.001; Student's t test, mean ± SEM).
(F) Quantification of the fluorescence intensity of individual BC vesicles in the TIRF plane. Shown are diagrams of 14 individual vesicles arranged from the most peripheral to the most central ones (see Figure 5D for positions). The distance distribution of vesicles measured from the cell edge is indicated. Notice the difference in the y axis scale. (n = 22 vesicles in two cells).
See also Movie S3.

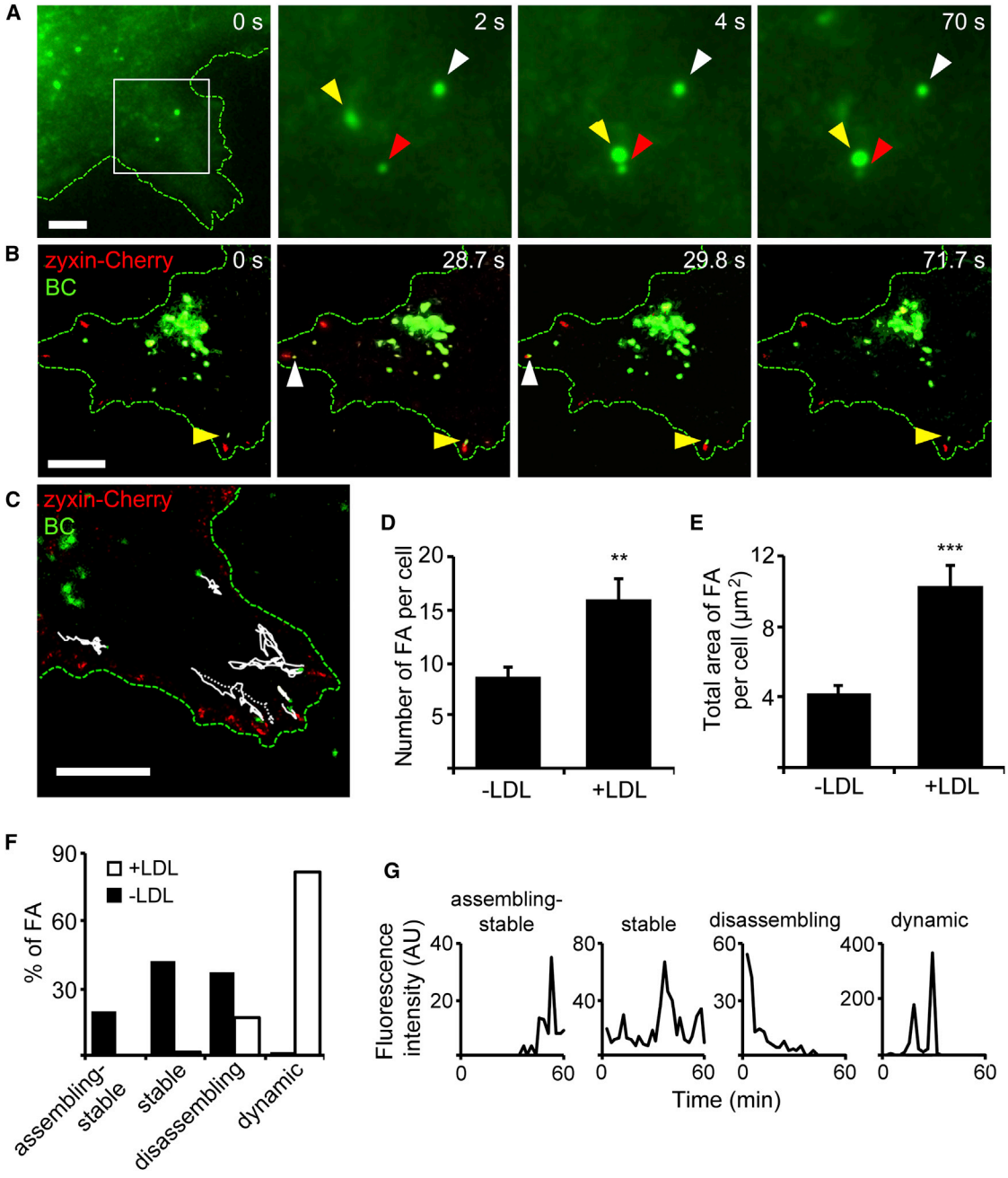

Figure 6. Delivery of BC-Harboring Organelles to FA and Modulation of FA by LDL

(A) Selected images from a time-lapse TIRF series showing a protrusion of the PM in A431 cell pulse-labeled with BC LN-LDL and chased for 2 hr. Dashed line indicates cell edge. The 2–70 s images show higher magnification of the area indicated in 0 s image. Images show stationary BC-positive vesicles (red and white arrowheads) and a moving BC vesicle (yellow arrowhead) joining the red vesicle. Scale bar, 5 μm.

(B) Confocal images from a movie obtained from BC LN-LDL pulse-labeled A431 cell overexpressing zyxin-Cherry. Images were acquired after a 3 hr chase. Arrowheads indicate BC vesicles communicating with zyxin-Cherry-positive focal adhesions. Dashed line indicates cell edge. Scale bar, 10 μm.

(C) An image from a similar time-lapse confocal series as in Figure 6B with trajectories of all the moving BC vesicles. Images were acquired at 1.1 s intervals for ~7 min after a 3 hr chase of BC LN-LDL. Dashed green line indicates cell edge. Scale bar, 10 μm.

(D and E) Quantification of FA number (D) and size (E) in A431 cells in the absence (−LDL) or presence of LDL (+LDL). Fixed cells were immunostained for vinculin and the amount and size of FA was quantified (n = 206–370 FA in 23–24 cells; ***$p < 0.001$; **$p < 0.01$; Student's t test, mean ± SEM).

(F) Quantification of FA dynamics. Shown are the fractions of different types of FA observed in A431 cells overexpressing GFP-paxillin. The cells were either loaded (+LDL) or not loaded (−LDL) with LDL. After 3 hr of chase, transfected cells were time-lapse imaged for 1 hr and the fluorescence intensity was quantified (n = 61–78 FA in 2–7 cells).

(G) Examples of fluorescence intensity fluctuation profiles used to classify FA into four subtypes. Notice the difference in the y axis scale.

See also Movies S4 and S5.

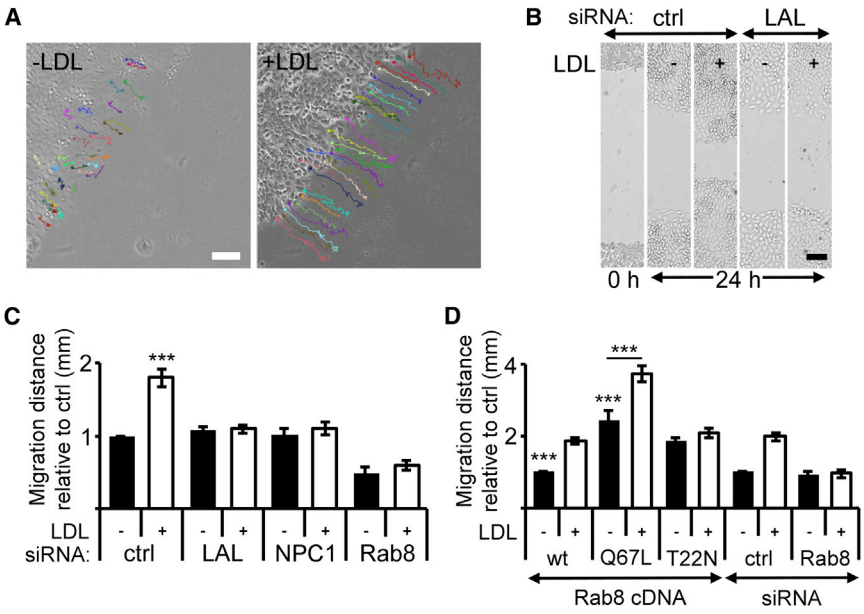

Figure 7. LDL-Derived Cholesterol Stimulates Cell Migration

(A) Wide-field images from the beginning of a movie of scratch-wounded A431 cells incubated in medium with (+LDL) or without LDL (−LDL). The cells were imaged every 20 min and the lines represent trajectories of individual cells after 10 hr of healing. Scale bar, 100 μm.

(B) Phase contrast images from a wound healing assay of A431. The cells were transfected with the indicated siRNAs. At t = 0 hr, the monolayer was scratched and cells were incubated in medium with (+) or without (−) LDL. After 24 hr, the extent of wound closure was analyzed. Scale bar, 100 μm.

(C) Quantification of the width of the wounds (n = 14–21; ***p < 0.001; Student's t test, mean ± SEM, compared to control −LDL). The results were normalized to control, which corresponds to 294 ± 4 μm distance.

(D) Quantification of wound healing in HT1080 cells. Wild-type (WT)-, Rab8 Q67L-, or Rab8 T22N-overexpressing cells or WT cells transfected with the indicated siRNAs were scratch-wounded, incubated in medium with (+) or without (−) LDL, and the wound closure was quantified after 24 hr (n = 11–12 [WT and stable transfectants]; n = 7–8 [siRNA-treated cells]; ***p < 0.001; Student's t test, mean ± SEM, compared to WT +LDL unless otherwise indicated). The results were normalized to control, which corresponds to 132 ± 10 μm distance.

See also Figure S5.

the number and dynamics of FA, and stimulated cell migration in an acid lipase, NPC1, and Rab8-dependent fashion argue that LDL cholesterol is an important regulator of FA dynamics in moving cells. This agrees with the high order of membrane lipids in FA (Gaus et al., 2006). Thus, in the future it will be important to reveal the precise mechanisms by which LDL cholesterol, potentially together with proteins cotransported in the cholesterol carriers, act to modulate FA and consequently promote cell migration and related processes dependent on FA dynamics.

EXPERIMENTAL PROCEDURES

Synthesis of BC LN

Twenty micromoles N,N′-dicyclohexylcarbodiimide and 4.1 μmol 4-dimethylaminopyridine were added to a solution of 5 μmol BC and 7.5 μmol linoleic acid in dry dichloromethane (2 ml). After stirring for 24 hr at room temperature, 10 μmol DCC, 4.1 μmol 4-dimethylaminopyridine, and 7.5 μmol linoleic acid were added. When the disappearance of BC was noted with thin-layer chromatography (TLC; hexane:ethyl acetate, 30:1), 3 ml water was added, and the product was extracted with dichloromethane. The organic layer was dried with anhydrous $MgSO_4$, the solvent was removed under vacuum, and the residue purified by flash chromatography on silica gel (elution with a gradient of hexane to hexane:ethyl acetate, 30:1) to afford 3.4 mg of BC LN (yield, 81%). The structure and purity of BC LN were confirmed by ^{1}H- and ^{13}C-NMR spectroscopy and high-resolution mass spectrometry.

LDL Preparation and Labeling

Human LDL was prepared from pooled plasma of four healthy volunteers by sequential ultracentrifugation as described (Goldstein et al., 1983). Fifty nanomoles BC LN in DMSO was used to label 1 mg LDL at 40°C for 2 hr followed by dialysis against 1mM EDTA in PBS. The protein concentration was determined using Bio-Rad protein assay. [^{3}H]-CL LDL complex was prepared similarly using 40 μCi [^{3}H]-CL (Sigma). Gel filtration chromatography was carried out with a Merck LaChrom FPLC. LDL was loaded on a Superose 6 10/300 GL column (GE Healthcare) equilibrated with PBS-EDTA at 0.5 ml/min; 0.5 ml fractions were collected and BC fluorescence was measured with a Wallac Victor 1420 (PerkinElmer). As shown in Figure 1B, BC LN associated with intact LDL particles after labeling.

Cell Culture, Transient Transfections, and Stable Cell Lines

For the description of cell lines and transfection procedures used in the study, see the Supplemental Experimental Procedures.

LDL Pulse-Chase Assay

A431 cells were incubated overnight with 50 μg/ml Alexa Fluor 568- or 647-dextran (Molecular Probes) in DMEM supplemented with 5% lipoprotein-deficient serum (LPDS, prepared as in Goldstein et al., 1983). Cells were then pulse-labeled for 2 hr (primary fibroblasts for 7 hr) with 50 μg/ml BC LN-LDL (or [^{3}H]-CL LDL or unlabeled LDL) in serum free (SF) medium, washed, and chased in SF medium for the times indicated in each experiment. Live-cell microscopy was used to follow the chase, and the fraction of BC residing in dextran-positive organelles was quantified. The uptake of BC LN-LDL was quantified from fixed cells by measuring total fluorescence of BC per cell. In some experiments, cells were chased in medium containing 2 μM nocodazole or 1 μM LatA (Sigma).

Plasmids

The cDNA constructs used in the study are described in the Supplemental Experimental Procedures.

Lipid Analysis

The cells were collected by scraping in a cold 2% NaCl and lipids were extracted as described (Bligh and Dyer, 1959). Samples were separated by TLC (hexane:diethyl ether:acetic acid, 80:20:1; or petroleum ether:diethyl ether:acetic acid, 60:40:1). Radioactive samples were scraped from the plate and quantified by scintillation counting, plates with fluorescent samples were scanned using FLA-9000 Starion (Fujifilm), and intensities were quantified from the images. To analyze BC LN and [^{3}H]-CL hydrolysis in vitro, 1 μg labeled LDL was incubated with postnuclear A431 homogenate (60 μg of protein) as described previously (Lusa and Somerharju, 1998). The lipids were then extracted and analyzed with TLC as above. To determine the arrival of LDL-derived cholesterol to the PM, cells were labeled with [^{3}H]-CL LDL, chased, and fixed with 4% PFA in 250 mM HEPES, 100 μM $CaCl_2$, and 100 μM $MgCl_2$ for 20 min. The cells were then oxidized with 1.5 U/ml cholesterol

oxidase (from *Streptomyces* sp., Calbiochem) in PBS at 37°C for 10 min. The cells were scraped, and the lipids were extracted and analyzed by scintillation counting or stained with filipin.

Immunofluorescence and Immunoelectron Microscopy

Immunofluorescence stainings were performed as described (Linder et al., 2007). Rab8 and Lamp 1 antibodies and filipin were used as described previously (Linder et al., 2007). In addition, mouse anti-CD63 (1:100, DSHB) and mouse anti-vinculin antibodies (1:1, VIIF9, a gift from Prof. Ismo Virtanen, University of Helsinki, Finland) were used. For immunoelectron microscopy, stable GFP-Rab8a overexpressing cells were LDL-loaded for 4 hr and fixed in 2% paraformaldehyde and 0.125% glutaraldehyde (Electron Microscopical Sciences) in 0.2 M phosphate buffer for 2 hr. Cells were processed for ultracryomicrotomy and double immunogold labeled using PAG10 and PAG15 (Cell Microscopy Center, Utrecht University, The Netherlands) as reported previously (Raposo et al., 2001). All samples were analyzed using a FEI CM120 electron microscope (FEI), and digital acquisitions were made with a numeric camera (Keen View, Soft Imaging System).

Image Acquisition

For live-cell imaging, cells were grown on glass-bottom dishes (Nunc LabTek or Greiner CELLview). The microscopes were equipped with environmental chambers with CO_2 supply. Alternatively, CO_2-independent medium (GIBCO) was used.

BC LN-LDL uptake and filipin were imaged with an IX70 inverted microscope (Olympus) equipped with a 40× oil immersion objective (1.35 NA), a Polychrome IV monochromator, and an Imago-QE camera (both TILL Photonics). For other wide field microscopy, a Nikon Eclipse Ti-E inverted microscope equipped with a Perfect Focus System, a motorized stage (both Nikon), and an iXon 885 EMCCD camera (Andor) was used (with 10×/0.30 NA or 40×/0.75 NA dry objectives or 63×/1.40 NA oil objective). TIRF imaging was performed with the same microscope with an argon laser (75 mW, Melles Griot) at 488 nm and an 100× oil immersion objective (1.49 NA). The microscope was controlled with NIS-Elements Advanced Research 3.1 (Nikon).

Confocal imaging was performed on a Leica TCS SP2 attached to a DM RXA2 upright microscope with 63× water or oil immersion objective (0.90 NA and 1.40 NA, respectively) or Leica TCS SP8 attached to a DMI 6000 inverted microscope with 63× water (1.20 NA) or glycerol (1.30 NA) objective. High frame-rate tracking was performed on the latter microscope using a resonant scanner. Data were acquired with LAS AF 3 (Leica).

Image Quantification

Quantifications were performed with Image-Pro Plus 5.1 (Media Cybernetics) or ImageJ (National Institutes of Health, Bethesda, MD, USA) for background subtracted images. Filipin fluorescence intensity was analyzed as described (Linder et al., 2007). For colocalization analysis, Mander's overlap coefficients were determined from single focal planes except when indicated that Pearson's coefficients were calculated. Vectorial motility of endosomes was determined from time-lapse sequences using the Image-Pro Plus "Track objects" function to measure the maximal distance traveled from the starting point. In wound healing studies, the shortest distance between the edges of the scratch was measured and the migration distance was obtained by subtracting the width at 24 hr from that at 0 hr.

To analyze PM arrival of BC, the total fluorescence intensity in the TIRF plane was assessed. For quantification of time-lapse TIRF images, fluorescence intensity and vesicle velocity were analyzed using ImageJ Manual tracking plugin. For FA quantification, FAs were thresholded and the "Analyze particles" function of ImageJ was used. FAs were classified based on the fluorescence intensity fluctuation profiles (Figure 6G): "assembling-stable," an appearing fluorescence signal that stabilizes; "stable," a persistent signal; "disassembling," a decreasing signal that does not reappear; and "dynamic," a rapid peaking of a local signal that disappears fast. For quantification of Rab8-positive vesicles or domains containing BC, Cherry-Rab8-positive punctae were thresholded as above for FA and the fraction containing BC fluorescence was quantified. For quantification of zyxin-Cherry and BC colocalization, BC vesicles were classified as immotile (docked) if the colocalization of the labels persisted $\geq$4 s or as interacting transiently when the labels either colocalized < 4 s or appeared side by side with no black pixels between them. For three-dimensional projections, images were deconvolved with Huygens Professional (SVI) and the renderings were made with Imaris 7.2 (Bitplane).

Immunoisolation of LE/LY

siRNA-transfected cells were LDL-loaded for 4 hr and lysed in 0.2% BSA, 2 mM EDTA, and protease inhibitors in PBS by passing through a 25 gauge needle. Lysates were cleared by centrifugation. Immunoisolations were carried out on equal amounts of total protein. LE/LY were captured by incubation overnight at 4°C with tosyl-activated Dynabeads (Invitrogen) precoupled to rabbit anti-NPC1 antibody (Novus Biologicals) or, for control, beads conjugated to an irrelevant antibody. Organelles were collected by magnetic separation and, after washing, bound material was solubilized in Laemmli sample buffer and resolved on 12% SDS-polyacrylamide gel followed by blotting against the following antibodies: rabbit anti-NPC1 (1:1,000), mouse anti-Rab8 (BD Transduction Laboratories, 1:1,200), and rabbit anti-actin (Sigma, 1:1,000). Primary antibodies were detected with Alexa Fluor 680-(Molecular probes, 1:10,000) or IRDye 800CW-conjugated (LI-COR Biosciences, 1:10,000) secondary antibodies and quantified on Odyssey CLx (LI-COR Biosciences) using Image Studio 2.0.

Wound Healing Assay

A431 or HT1080 cells were grown to confluency in complete medium before manually scratching the monolayer with a pipette tip. Cells were then placed into serum-free medium with or without LDL and the width of the scratch-wound region was imaged at 0 hr and 24 hr. When indicated, the medium was supplemented with 10 μg/ml mitomycin C (Sigma). For time-lapse wound healing studies, the images were acquired every 20 min for 10 hr after scratching.

Statistical Analysis

Statistical significance was determined by two-tailed Student's t test. Differences were considered statistically significant at $p < 0.05$. Results are expressed as mean ± SEM of the indicated number of observations.

SUPPLEMENTAL INFORMATION

Supplemental Information includes Supplemental Experimental Procedures, five figures, one table, and five movies and can be found with this article online at http://dx.doi.org/10.1016/j.devcel.2013.09.016.

ACKNOWLEDGMENTS

We thank Zaiguo Li and Vjekoslav Dekaris for help in preparing BC LN; Ana Maria Cuervo, Gillian Griffiths, and Maria Vartiainen for cDNA contructs; Matti Jauhiainen, Jari Metso, and Emmi Pakarinen for LDL purification; Mikko Liljeström and Biomedicum Imaging Unit for help with microscopy; and Anna Uro and Pipsa Kaipainen for technical support. This work was financially supported by the Academy of Finland (250081 to K.K. and 131489, 218066, and 263841 to E.I.), Sigrid Juselius Foundation (to E.I.), and the Finnish Medical Foundation (to E.I. and R.B.).

Received: May 29, 2013
Revised: August 9, 2013
Accepted: September 16, 2013
Published: October 24, 2013

REFERENCES

Bligh, E.G., and Dyer, W.J. (1959). A rapid method of total lipid extraction and purification. Can. J. Biochem. Physiol. *37*, 911–917.

Blom, T., Bäck, N., Mutka, A.L., Bittman, R., Li, Z., de Lera, A., Kovanen, P.T., Diczfalusy, U., and Ikonen, E. (2010). FTY720 stimulates 27-hydroxycholesterol production and confers atheroprotective effects in human primary macrophages. Circ. Res. *106*, 720–729.

Brown, M.S., and Goldstein, J.L. (1986). A receptor-mediated pathway for cholesterol homeostasis. Science *232*, 34–47.

Bryant, D.M., Datta, A., Rodríguez-Fraticelli, A.E., Peränen, J., Martín-Belmonte, F., and Mostov, K.E. (2010). A molecular network for de novo generation of the apical surface and lumen. Nat. Cell Biol. *12*, 1035–1045.

Chabrillat, M.L., Wilhelm, C., Wasmeier, C., Sviderskaya, E.V., Louvard, D., and Coudrier, E. (2005). Rab8 regulates the actin-based movement of melanosomes. Mol. Biol. Cell *16*, 1640–1650.

Chen, H., Yang, J., Low, P.S., and Cheng, J.X. (2008). Cholesterol level regulates endosome motility via Rab proteins. Biophys. J. *94*, 1508–1520.

Choudhury, A., Sharma, D.K., Marks, D.L., and Pagano, R.E. (2004). Elevated endosomal cholesterol levels in Niemann-Pick cells inhibit rab4 and perturb membrane recycling. Mol. Biol. Cell *15*, 4500–4511.

Deffieu, M.S., and Pfeffer, S.R. (2011). Niemann-Pick type C 1 function requires lumenal domain residues that mediate cholesterol-dependent NPC2 binding. Proc. Natl. Acad. Sci. USA *108*, 18932–18936.

Donovan, K.W., and Bretscher, A. (2012). Myosin-V is activated by binding secretory cargo and released in coordination with Rab/exocyst function. Dev. Cell *23*, 769–781.

Du, X., Kumar, J., Ferguson, C., Schulz, T.A., Ong, Y.S., Hong, W., Prinz, W.A., Parton, R.G., Brown, A.J., and Yang, H. (2011). A role for oxysterol-binding protein-related protein 5 in endosomal cholesterol trafficking. J. Cell Biol. *192*, 121–135.

Du, X., Kazim, A.S., Brown, A.J., and Yang, H. (2012). An essential role of Hrs/Vps27 in endosomal cholesterol trafficking. Cell Rep. *1*, 29–35.

Du, X., Kazim, A.S., Dawes, I.W., Brown, A.J., and Yang, H. (2013). The AAA ATPase VPS4/SKD1 regulates endosomal cholesterol trafficking independently of ESCRT-III. Traffic *14*, 107–119.

Fukuda, M. (2013). Rab27 effectors, pleiotropic regulators in secretory pathways. Traffic *14*, 949–963.

Gallala, H.D., and Sandhoff, K. (2011). Biological function of the cellular lipid BMP-BMP as a key activator for cholesterol sorting and membrane digestion. Neurochem. Res. *36*, 1594–1600.

Ganley, I.G., and Pfeffer, S.R. (2006). Cholesterol accumulation sequesters Rab9 and disrupts late endosome function in NPC1-deficient cells. J. Biol. Chem. *281*, 17890–17899.

Gaus, K., Le Lay, S., Balasubramanian, N., and Schwartz, M.A. (2006). Integrin-mediated adhesion regulates membrane order. J. Cell Biol. *174*, 725–734.

Goldstein, J.L., Basu, S.K., and Brown, M.S. (1983). Receptor-mediated endocytosis of low-density lipoprotein in cultured cells. Methods Enzymol. *98*, 241–260.

Hattula, K., Furuhjelm, J., Arffman, A., and Peränen, J. (2002). A Rab8-specific GDP/GTP exchange factor is involved in actin remodeling and polarized membrane transport. Mol. Biol. Cell *13*, 3268–3280.

Hattula, K., Furuhjelm, J., Tikkanen, J., Tanhuanpää, K., Laakkonen, P., and Peränen, J. (2006). Characterization of the Rab8-specific membrane traffic route linked to protrusion formation. J. Cell Sci. *119*, 4866–4877.

Hölttä-Vuori, M., Määttä, J., Ullrich, O., Kuismanen, E., and Ikonen, E. (2000). Mobilization of late-endosomal cholesterol is inhibited by Rab guanine nucleotide dissociation inhibitor. Curr. Biol. *10*, 95–98.

Hölttä-Vuori, M., Tanhuanpää, K., Möbius, W., Somerharju, P., and Ikonen, E. (2002). Modulation of cellular cholesterol transport and homeostasis by Rab11. Mol. Biol. Cell *13*, 3107–3122.

Hölttä-Vuori, M., Uronen, R.L., Repakova, J., Salonen, E., Vattulainen, I., Panula, P., Li, Z., Bittman, R., and Ikonen, E. (2008). BODIPY-cholesterol: a new tool to visualize sterol trafficking in living cells and organisms. Traffic *9*, 1839–1849.

Ikonen, E. (2008). Cellular cholesterol trafficking and compartmentalization. Nat. Rev. Mol. Cell Biol. *9*, 125–138.

Jansen, M., Ohsaki, Y., Rita Rega, L., Bittman, R., Olkkonen, V.M., and Ikonen, E. (2011). Role of ORPs in sterol transport from plasma membrane to ER and lipid droplets in mammalian cells. Traffic *12*, 218–231.

Keller, P., Toomre, D., Díaz, E., White, J., and Simons, K. (2001). Multicolour imaging of post-Golgi sorting and trafficking in live cells. Nat. Cell Biol. *3*, 140–149.

Khandelwal, P., Prakasam, H.S., Clayton, D.R., Ruiz, W.G., Gallo, L.I., van Roekel, D., Lukianov, S., Peränen, J., Goldenring, J.R., and Apodaca, G. (2013). A Rab11a-Rab8a-Myo5B network promotes stretch-regulated exocytosis in bladder umbrella cells. Mol. Biol. Cell *24*, 1007–1019.

Knödler, A., Feng, S., Zhang, J., Zhang, X., Das, A., Peränen, J., and Guo, W. (2010). Coordination of Rab8 and Rab11 in primary ciliogenesis. Proc. Natl. Acad. Sci. USA *107*, 6346–6351.

Kobayashi, T., Vischer, U.M., Rosnoblet, C., Lebrand, C., Lindsay, M., Parton, R.G., Kruithof, E.K., and Gruenberg, J. (2000). The tetraspanin CD63/lamp3 cycles between endocytic and secretory compartments in human endothelial cells. Mol. Biol. Cell *11*, 1829–1843.

Kwon, H.J., Abi-Mosleh, L., Wang, M.L., Deisenhofer, J., Goldstein, J.L., Brown, M.S., and Infante, R.E. (2009). Structure of N-terminal domain of NPC1 reveals distinct subdomains for binding and transfer of cholesterol. Cell *137*, 1213–1224.

Lebrand, C., Corti, M., Goodson, H., Cosson, P., Cavalli, V., Mayran, N., Fauré, J., and Gruenberg, J. (2002). Late endosome motility depends on lipids via the small GTPase Rab7. EMBO J. *21*, 1289–1300.

Letinic, K., Sebastian, R., Toomre, D., and Rakic, P. (2009). Exocyst is involved in polarized cell migration and cerebral cortical development. Proc. Natl. Acad. Sci. USA *106*, 11342–11347.

Linder, M.D., Uronen, R.L., Hölttä-Vuori, M., van der Sluijs, P., Peränen, J., and Ikonen, E. (2007). Rab8-dependent recycling promotes endosomal cholesterol removal in normal and sphingolipidosis cells. Mol. Biol. Cell *18*, 47–56.

Linder, M.D., Mäyränpää, M.I., Peränen, J., Pietilä, T.E., Pietiäinen, V.M., Uronen, R.L., Olkkonen, V.M., Kovanen, P.T., and Ikonen, E. (2009). Rab8 regulates ABCA1 cell surface expression and facilitates cholesterol efflux in primary human macrophages. Arterioscler. Thromb. Vasc. Biol. *29*, 883–888.

Lombardi, D., Soldati, T., Riederer, M.A., Goda, Y., Zerial, M., and Pfeffer, S.R. (1993). Rab9 functions in transport between late endosomes and the trans Golgi network. EMBO J. *12*, 677–682.

Lusa, S., and Somerharju, P. (1998). Degradation of low density lipoprotein cholesterol esters by lysosomal lipase in vitro. Effect of core physical state and basis of species selectivity. Biochim. Biophys. Acta *1389*, 112–122.

Möbius, W., van Donselaar, E., Ohno-Iwashita, Y., Shimada, Y., Heijnen, H.F., Slot, J.W., and Geuze, H.J. (2003). Recycling compartments and the internal vesicles of multivesicular bodies harbor most of the cholesterol found in the endocytic pathway. Traffic *4*, 222–231.

Nachury, M.V., Loktev, A.V., Zhang, Q., Westlake, C.J., Peränen, J., Merdes, A., Slusarski, D.C., Scheller, R.H., Bazan, J.F., Sheffield, V.C., and Jackson, P.K. (2007). A core complex of BBS proteins cooperates with the GTPase Rab8 to promote ciliary membrane biogenesis. Cell *129*, 1201–1213.

Ostrowski, M., Carmo, N.B., Krumeich, S., Fanget, I., Raposo, G., Savina, A., Moita, C.F., Schauer, K., Hume, A.N., Freitas, R.P., et al. (2010). Rab27a and Rab27b control different steps of the exosome secretion pathway. Nat. Cell Biol. *12*, 19–30.

Peränen, J., Auvinen, P., Virta, H., Wepf, R., and Simons, K. (1996). Rab8 promotes polarized membrane transport through reorganization of actin and microtubules in fibroblasts. J. Cell Biol. *135*, 153–167.

Pols, M.S., and Klumperman, J. (2009). Trafficking and function of the tetraspanin CD63. Exp. Cell Res. *315*, 1584–1592.

Raposo, G., Tenza, D., Murphy, D.M., Berson, J.F., and Marks, M.S. (2001). Distinct protein sorting and localization to premelanosomes, melanosomes, and lysosomes in pigmented melanocytic cells. J. Cell Biol. *152*, 809–824.

Röhrl, C., Meisslitzer-Ruppitsch, C., Bittman, R., Li, Z., Pabst, G., Prassl, R., Strobl, W., Neumüller, J., Ellinger, A., Pavelka, M., and Stangl, H. (2012). Combined light and electron microscopy using diaminobenzidine photooxidation to monitor trafficking of lipids derived from lipoprotein particles. Curr. Pharm. Biotechnol. *13*, 331–340.

Roland, J.T., Kenworthy, A.K., Peränen, J., Caplan, S., and Goldenring, J.R. (2007). Myosin Vb interacts with Rab8a on a tubular network containing EHD1 and EHD3. Mol. Biol. Cell *18*, 2828–2837.

Roland, J.T., Lapierre, L.A., and Goldenring, J.R. (2009). Alternative splicing in class V myosins determines association with Rab10. J. Biol. Chem. *284*, 1213–1223.

Roland, J.T., Bryant, D.M., Datta, A., Itzen, A., Mostov, K.E., and Goldenring, J.R. (2011). Rab GTPase-Myo5B complexes control membrane recycling and epithelial polarization. Proc. Natl. Acad. Sci. USA *108*, 2789–2794.

Santiago-Tirado, F.H., Legesse-Miller, A., Schott, D., and Bretscher, A. (2011). PI4P and Rab inputs collaborate in myosin-V-dependent transport of secretory compartments in yeast. Dev. Cell *20*, 47–59.

Sato, T., Mushiake, S., Kato, Y., Sato, K., Sato, M., Takeda, N., Ozono, K., Miki, K., Kubo, Y., Tsuji, A., et al. (2007). The Rab8 GTPase regulates apical protein localization in intestinal cells. Nature *448*, 366–369.

Slotte, J.P., and Bierman, E.L. (1988). Fatty acid specificity of the lysosomal acid cholesterol esterase in intact human arterial smooth muscle cells. Biochim. Biophys. Acta *958*, 308–312.

Urano, Y., Watanabe, H., Murphy, S.R., Shibuya, Y., Geng, Y., Peden, A.A., Chang, C.C., and Chang, T.Y. (2008). Transport of LDL-derived cholesterol from the NPC1 compartment to the ER involves the trans-Golgi network and the SNARE protein complex. Proc. Natl. Acad. Sci. USA *105*, 16513–16518.

Vaibhava, V., Nagabhushana, A., Chalasani, M.L., Sudhakar, C., Kumari, A., and Swarup, G. (2012). Optineurin mediates a negative regulation of Rab8 by the GTPase-activating protein TBC1D17. J. Cell Sci. *125*, 5026–5039.

Vale, R.D., and Fletterick, R.J. (1997). The design plan of kinesin motors. Annu. Rev. Cell Dev. Biol. *13*, 745–777.

Walter, M., Davies, J.P., and Ioannou, Y.A. (2003). Telomerase immortalization upregulates Rab9 expression and restores LDL cholesterol egress from Niemann-Pick C1 late endosomes. J. Lipid Res. *44*, 243–253.

Westlake, C.J., Baye, L.M., Nachury, M.V., Wright, K.J., Ervin, K.E., Phu, L., Chalouni, C., Beck, J.S., Kirkpatrick, D.S., Slusarski, D.C., et al. (2011). Primary cilia membrane assembly is initiated by Rab11 and transport protein particle II (TRAPPII) complex-dependent trafficking of Rabin8 to the centrosome. Proc. Natl. Acad. Sci. USA *108*, 2759–2764.

Wojtanik, K.M., and Liscum, L. (2003). The transport of low density lipoprotein-derived cholesterol to the plasma membrane is defective in NPC1 cells. J. Biol. Chem. *278*, 14850–14856.

Yoshimura, S., Egerer, J., Fuchs, E., Haas, A.K., and Barr, F.A. (2007). Functional dissection of Rab GTPases involved in primary cilium formation. J. Cell Biol. *178*, 363–369.